Chemical Engineering Journal 440 (2022) 135707

Contents lists available at ScienceDirect

Chemical Engineering Journal

journal homepage: www.elsevier.com/locate/cej

Albero: An alternative natural material for solar energy storage by the calcium-looping process

Virginia Moreno [a], Juan Arcenegui-Troya [a], Pedro Enrique Sánchez-Jiménez [a,b,*], Antonio Perejón [a,b,*], Ricardo Chacartegui [c], José Manuel Valverde [d], Luis Allan Pérez-Maqueda [a,*]

[a] Instituto de Ciencia de Materiales de Sevilla, C.S.I.C.-Universidad de Sevilla, C. Américo Vespucio, 49, 41092 Sevilla, Spain
[b] Departamento de Química Inorgánica, Facultad de Química, Universidad de Sevilla, 41012 Sevilla, Spain
[c] Departamentto de Ingeniería Energética, Escuela Técnica Superior de Ingenieros, Universidad de Sevilla, 41092 Sevilla, Spain
[d] Departamento de Electrónica y Electromagnetismo, Facultad de Física, Universidad de Sevilla, 41012 Sevilla, Spain

ARTICLE INFO

Keywords:
Albero
Limestone
Thermochemical energy storage
Calcium-Looping
Solar absorptance

ABSTRACT

Large-scale thermochemical energy storage (TCES) is gaining relevance as an alternative to current thermal energy storage systems in Concentrated Solar Power plants. Among the different systems, the reversible reaction between CaO and CO_2 stands out due to the wide availability and low cost of the raw material: limestone. Direct solar absorption of the storage media would improve the efficiency of solar-to-thermal energy storage due to reduced thermal transfer barriers, but the solar optical absorption of $CaCO_3$ is poor. In this work, we propose the use of a Ca-rich calcarenite sedimentary rock so-called albero as an alternative to limestone. We demonstrate that this reddish material exhibits an average solar absorptance that is approximately ten times larger than limestone. Moreover, the multicycle carbonation/calcination performance under different experimental conditions has been studied by thermogravimetry, and similar values to those exhibited for limestone have been obtained. Besides, the material is cheap (6 €/ton), and simulations showed that the use of this material would significantly improve the overall CaL-CSP efficiency at the industrial level.

1. Introduction

The large-scale replacement of fossil fuel based power plants by renewable energies is key in the strategy of the EU to attain climate neutrality in the next decades [1,2]. However, the intrinsic intermittency of renewable energies sources, such as solar and wind, hinders the match between supply and demand. Consequently, most-power generation is still based on fossil fuel based power plants, which emissions of greenhouse gases are still over the limits established in the Paris Agreement [3]. Another arising problem is the unprecedented expansion of grid-connected solar photovoltaic systems that is already producing over generation issues in California and Australia [4].

Thus, the deployment of massive energy storage systems is needed to store the energy produced when solar or wind is available and use it under demand independently of weather conditions. In this sense, the calcium looping (CaL) process, based on the reversible reaction between calcium oxide (CaO) and carbon dioxide (CO_2), has been recently proposed for the thermochemical energy storage (TCES) of concentrated solar power (CSP) [5–11]. In the CaL-CSP scheme, solar energy is used to drive the endothermic decomposition of $CaCO_3$ into CaO and CO_2 at high temperatures (950 °C) in a solar reactor (calciner). When thermal power generation is required, CaO and CO_2 are transported to another reactor (carbonator) to yield the exothermic carbonation reaction [5–8,12]. After carbonation, the $CaCO_3$ is circulated back to the solar receiver to regenerate the CaO for its use in a new cycle. Carbonation is carried out at high temperature and high CO_2 pressure well above the stoichiometric ratio. The CO_2 in excess at high temperature and high partial pressure is conducted from the carbonator to a gas turbine for power generation [13,14].

Two general schemes of CaL-CSP integration have been proposed (Fig. 1), mainly distinguished by the conditions under which calcination is carried out. In both schemes, carbonation is conducted under CO_2 at high temperatures (>800 °C) to achieve high thermoelectric efficiency [5,15]. In a first scheme (Fig. 1a), calcination of $CaCO_3$ is carried out

* Corresponding authors.
E-mail addresses: pedro.enrique@icmse.csic.es (P. Enrique Sánchez-Jiménez), aperejon@us.es (A. Perejón), maqueda@cica.es (L. Allan Pérez-Maqueda).

https://doi.org/10.1016/j.cej.2022.135707
Received 22 September 2021; Received in revised form 4 March 2022; Accepted 7 March 2022
Available online 8 March 2022

under an inert gas at a relative low temperature (around 750 °C), which allows using conventional solar receivers, in which the heat transfer fluid is heated indirectly. However, this integration scheme would require the use of a separation system for the inert gas/CO_2 mixture released in the solar receiver, which imposes an energy penalty and increases the cost of the technology. [16–19]. A second option (Fig. 1b) is performing calcination under CO_2, at a temperature of 950 °C to achieve full calcination in the short residence times (in the order of several minutes) required in practice. Calcination under CO_2 would allow using a closed CO_2 circuit for calcination, carbonation and power generation thus reducing the technical complexity of the integration [5,6,13].

The global deployment of the CaL-CSP technology relies on the availability of environmentally friendly, non-toxic, and cheap $CaCO_3$ rich materials. A large variety of materials has been proposed for their use as CaO precursors, including food waste, industrial by-products and natural minerals (limestone and dolomite) [16,20–24]. Among all of them, limestone stands out as the most promising material for its low cost (10 €/ton), $CaCO_3$ content (close to 100%), and abundance.

One of the main drawbacks of the CaL-CSP integration is the sintering-induced deactivation of CaO particles at high temperatures, further aggravated in the CO_2-rich environment. An extensive sintering of CaO particles deteriorates carbonation reactivity in any subsequent cycle [15,25,26]. Moreover, for particles larger than 20–30 μm, pore plugging also severely limits carbonation at high temperature under CO_2; it is caused by the rapid formation of a $CaCO_3$ blocking layer that prevents the carbonation of the unreacted inner CaO core [27–29]. The progressive loss of CaO reactivity could be offset by the continuous renewal of the spent sorbent, but this would increase the energy penalty and cost of the technology [30]. Therefore, much effort has been devoted to developing strategies for preventing CaO deactivation. The methods proposed include chemical and thermal pretreatments, CaO modification by additives and steam injection. Thus, chemical and thermal treatments lead to an enhancement in the reactivity of the material of 22–39 %, while the use of steam has been proven to increase reactivity up to 50 % [31–35].

Another issue to overcome in the application of the CaL process to store energy in CSP plants is the poor optical absorption capability of limestone [18,36–38] and other proposed materials [39–41]. Limestone can be hardly heated by direct solar radiation. Instead, indirect solar particle receivers are used, in which heat is transferred from the surface of a collector to a tube wall where the material is contained [42,43]. These collectors present a number of drawbacks related to heat losses and thermal resistance that reduce the overall efficiency of the plant [44–48]. Thus, new advanced direct solar absorption technologies are under investigation [49–53]. The direct interaction of sunlight with the

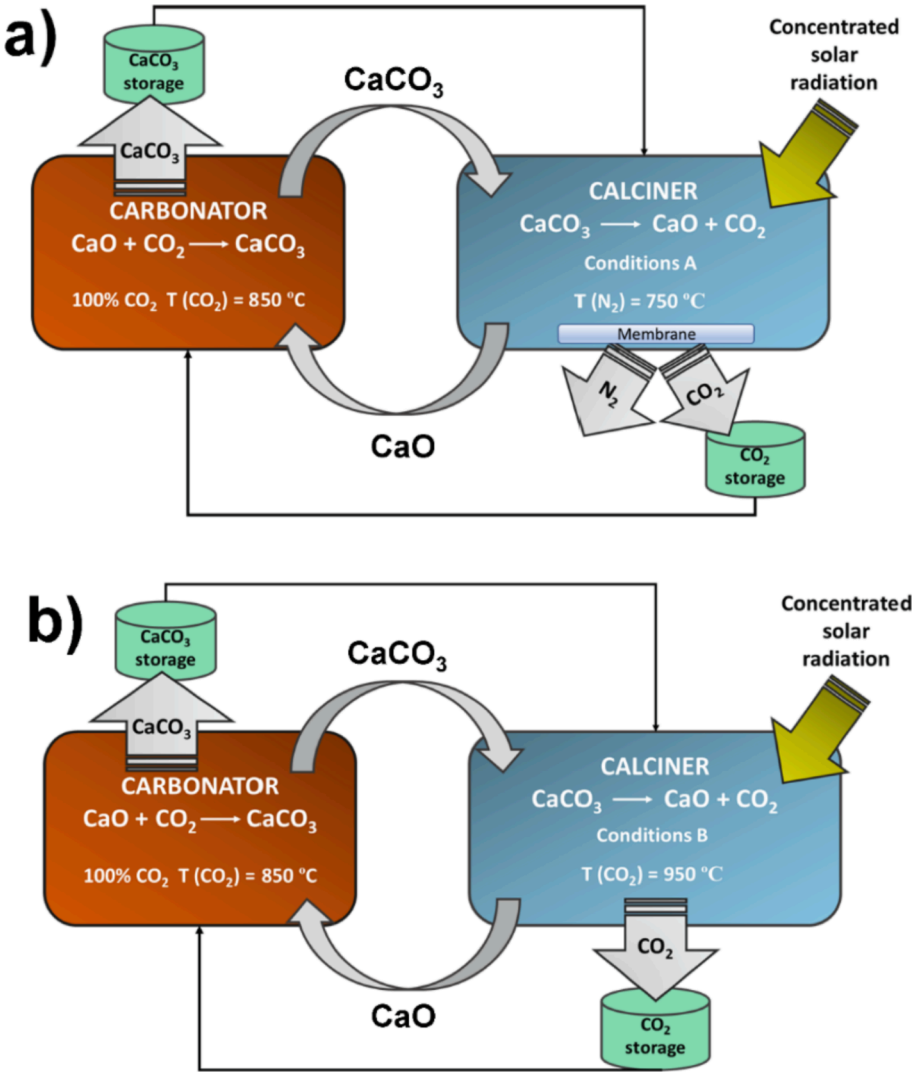

Fig. 1. Schematic representation of the CaL-CSP integration. In a) calcination is carried out in inert gas (CSP-N_2-calc), while in b) it is conducted in CO_2 (CSP-CO_2-calc).

Ca-based material would improve the efficiency of heat utilization by reducing thermal resistance and exergy losses. However, a significant improvement of the poor solar optical absorption of $CaCO_3$ is still required. This has been the objective of several recent works, in which CaO-based composites have been prepared by adding small amounts of Fe and Mn dopants in the form of metal oxides [54–57], leading to colored samples that become darker as the amount of iron and manganese oxides are raised. A remarkable improvement in the optical absorption of these synthetic samples has been reported since the dopant oxides can absorb a broadband sunlight spectrum.

In this work, the novelty consists in the study of naturally occuring albero as a material for thermochemical energy storage by means of the CaL process. Albero is a calcarenite material abundantly available, cheap (6 €/ton) and non-toxic, with a high $CaCO_3$ content. A comparative study between albero and limestone has been conducted, paying attention to their optical properties and multicycle performance tested in conditions compatible with the two CaL schemes aforementioned. The results of this work contribute to the potential use of albero in the CaL-CSP integration utilizing direct solar absorption technologies.

2. Materials and methods

2.1. Materials

The samples of albero studied in this work were supplied by Hermanos Salguero quarry (Alcalá de Guadaíra, Spain). Two distinct types of albero, locally designated as grancilla and garbancillo, were used. Albero consists mainly of calcite, quartz, and phyllosilicates. It exhibits a yellowish color due to the presence of small amounts of goethite, which is a Fe-oxo-hydroxide with the chemical formula FeO(OH). Thus, its color depends on the concentration of goethite and it becomes darker upon calcination since goethite transforms into hematite. The size distribution of the particles employed in the CaL process plays an important role on the multicyclic performance of limestone [25,26]. When calcination is carried out under an inert gas (CSP-N_2-calc conditions in our work as detailed below), CaO deactivation by pore plugging is a relevant limiting mechanism for particles of size above around 50 μm. To avoid this undesirable effect, the samples were sieved to particle sizes lower than 45 μm [28].

2.2. Particle size measurements

Particle size distributions (PSDs) were measured by laser diffraction analysis using a Mastersizer 2000 equipment (Malvern). The device uses the technique of laser diffraction to measure the size of particles (0.02 to 2000 μm) from the intensity of light scattered as the laser beam passes through a dispersed particulate sample with a data acquisition rate of 1 kHz. The samples were dispersed in deionized water and sonicated in an ultrasonic bath for 30 min to remove possible particle aggregates.

2.3. Multycicle measurements

Multicycle CaL-CSP tests were run in a thermogravimetric analyser TA instrument Q5000IR, provided with a highly sensitive balance (<0.1 μm) and a furnace heated by IR halogen lamps. IR heating allows for high heating and cooling rates, up to 300 °C min^{-1}, as well as stable isotherms. Fast heating/cooling rates are needed to mimic realistic conditions since the material would be quickly circulated between reactors at different temperatures. Table 1 shows the multicycle carbonation/calcination conditions tested in this work.

Table 1
Multicycle carbonation/calcination tests used in this work.

	Calcination	Carbonation
CSP-N_2-calc	N_2 at 750 °C	CO_2 at 850 °C
CSP-CO_2-calc	CO_2 at 950 °C	CO_2 at 850 °C

As stated, these conditions were taken as potential design conditions of CaL-CSP plants based on tower technology. The use of an inert gas in the calcination allows reducing CO_2 partial pressure and calcination turning temperature. It allows the use of lower temperatures in the solar receiver that imply reducing radiation losses significantly. In section 3.3, the impact on a potential scale-up plant, extracted from [5], working with these materials and operating conditions is analysed.

Both calcination and carbonation stages lasted 5 min to mimic the short residence times expected in the calciner and the carbonator. Small amounts of sample (10 mg) were used to avoid effects related to gas diffusion resistance through the samples [53]. Multicycle tests conducted under CSP-N_2-calc conditions were initiated with a ramp from room temperature up to 750 °C at 300 °C min^{-1} in nitrogen to start a calcination stage that lasted 5 min. Afterwards, the temperature was increased up to 850 °C and the atmosphere switched to CO_2 (purity grade 99.998%) to carry out the carbonation stage for 5 min. Once the 5-min carbonation stage finished, the temperature was decreased to 750 °C and the cycle was repeated 19 times. On the other hand, the experiments run in CSP-CO_2-calc conditions started with a calcination step, heating the sample from room temperature up to 950 °C at 300 °C min^{-1} in CO_2. After a 5 min-lasting calcination stage, the temperature was decreased to 850 °C and carbonation was carried out in CO_2 for 5 min. Once the carbonation was over, the temperature was raised to 950 °C to repeat the cycle 19 times.

2.4. X-Ray diffraction

XRD measurements of the samples were acquired using a Rigaku Miniflex diffractometer with a Ni filtered CuKα radiation (λ = 1.5406 Å) working at 40 kV and 15 mA in the 2θ range from 10° to 90°.

2.5. XRF analysis

X-ray microfluorescene (XRF) was used to obtain the elemental composition of the powdered samples using an Eagle III Micro XRF instrument (EDAX, New Jersey, USA) equipped with an X-ray anticathode 50 W rhodium tube and an energy dispersive X-ray detector.

2.6. SEM images

The microstructure of the samples was studied using scanning electron microscope (SEM) Hitachi S4800, which is a cold cathode field emission microscope that allows imaging the morphology and surface texture of samples with a resolution of 1 nm at 15 kV. SEM micrographs were taken before and after the calcination/carbonation cycles. Before SEM, the samples were sputtered coated with a thin layer of gold employing an Emitech K550 Telstar sputter-coating equipment. Fig. S1 includes SEM micrographs of as received garbancillo and grancilla.

2.7. Absorptance measurements

Ultraviolet–Visible-Near infrared (UV–Vis-NIR) absorptance tests were conducted at room temperature in the 300–2000 nm range with a spectrophotometer Agilent Cary 5000 from Agilent Technologies, by using an integrating sphere in this range. The full wavelength range was scanned at 1 nm intervals. The powder was packed into a sample cell and compacted for the measurements. Solar irradiance is affected by several components called direct, scattered (diffused) and global (or total) components. This parameter is measured by the unit air mass (AM). In this work, the solar-weighted absorptivity of the samples was calculated using the AM1.5Global (AM1.5G), being the standard spectrum at the Earth's surface.

2.8. Emissivity of the samples

Emissivity measurements were performed using an optris PI 450i infrared camera (Berlin, Germany), with a measurement speed of 80 Hz and an optical resolution of 382 × 288 pixels providing real-time, high-speed thermographic images in the spectral range 8–14 μm. The camera offers a temperature range of −20 °C to 1500 °C. A tubular furnace was employed for heating up the samples at a constant rate of 10 °C/min using a Euroterm 3216 PID controller. To monitor the local temperature, an n-type thermocouple was in direct contact with the sample (previously prepared in pellet form). During the measurements, the furnace was heated to the desired temperature and maintained for 30 min to reach equilibrium. Then, the emissivity of the sample was measured. The emissivity was computed assuming that the temperature measured in the thermocouple was the same than the temperature of the sample.

3. Results and discussion

3.1. Samples characterisation

Fig. 2 shows the PSDs measured for the samples tested in our work, which exhibit peaks around 16 μm and 28 μm for garbancillo and grancilla, respectively.

Chemical composition of the samples was determined by XRF analysis. Elemental composition of the samples after calcination is detailed in Table 2. As can be observed, the main elements present in the samples are calcium, around 60 wt%, and oxygen, around 30 wt%. As mentioned above, the yellowish color of albero is mainly ascribed to its iron content, representing approximately 2–3 wt%. Moreover, the samples also contain small amounts of silicon and aluminum from quartz and phyllosilicates.

Fig. 3 shows the X-ray diffractograms of the samples. The intensity is represented in square root to make the phases that are in smaller proportion more noticeable. The same phases are present in both patterns, albeit the relative intensity of the peaks differs from one to another. As expected, calcite is the predominant phase in the samples. Small amounts of quartz and goethite are also observed.

Fig. 4 shows pictures of the samples as received and after calcination at 900 °C. A limestone sample (supplied by Omya Clariana) is included for comparison purposes. As may be observed, the calcined samples exhibit a much darker color as compared with the raw ones. Color change can be explained by the transformation from goethite to hematite starting at ~ 250 °C with a chromatic change from yellowish to brown-reddish [58]. In addition, there is a mass loss associated to this transformation.

Fig. 5a shows the optical absorptance spectrum measured for garbancillo, grancilla and limestone. The spectral absorption $A(\lambda)$ of the

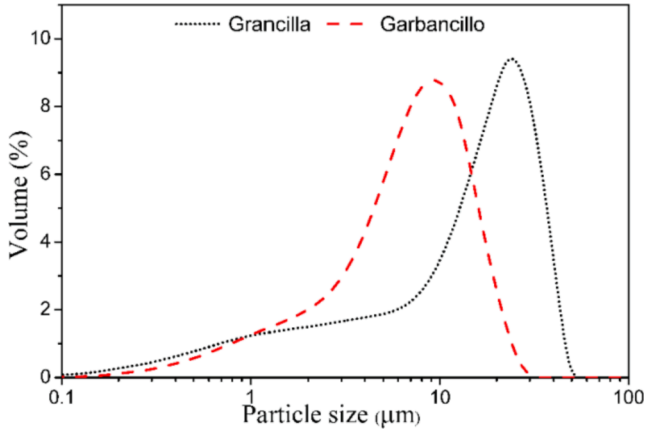

Fig. 2. Particle size distributions of the albero samples.

Table 2
Results of X-Ray fluorescence analysis of garbancillo and grancilla after calcination.

Sample	wt (%)					
	Si	Fe	Ca	Al	O	Others
Garbancillo	3.55	3.37	60.86	0.67	30.78	0.71
Grancilla	3.13	2.35	62.55	0.63	30.58	0.73

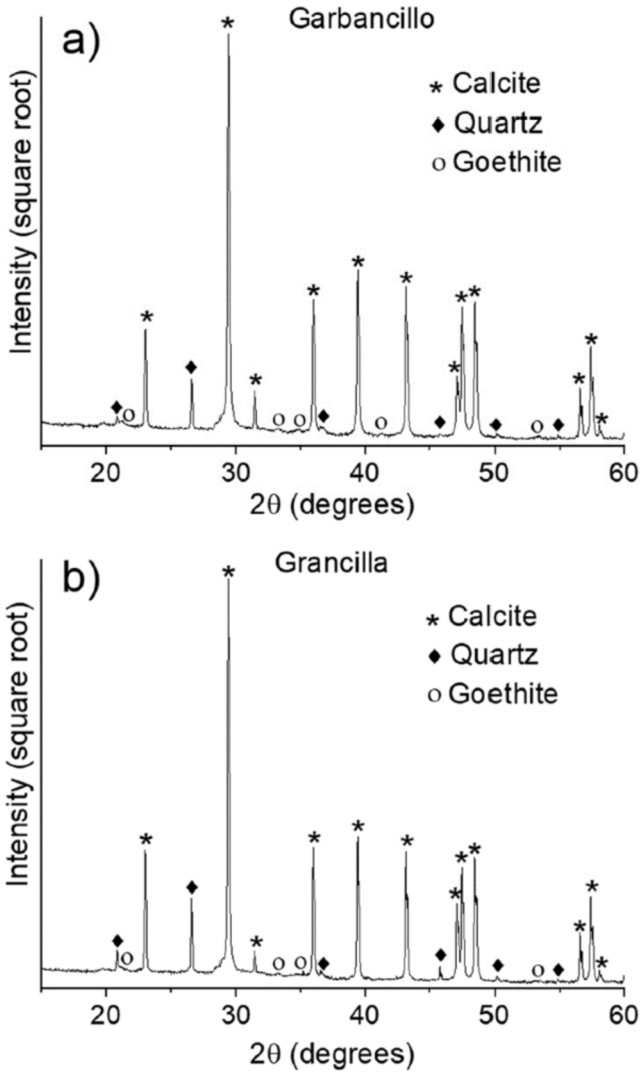

Fig. 3. XRD patterns measured for a) garbancillo and b) grancilla.

samples was calculated according to the following equation:

$$A(\lambda) = 100\% - R(\lambda) \quad (1)$$

where λ stands for the wavelength of the radiation and $R(\lambda)$ is the reflectance of the sample. A useful physical property to assess the solar radiation absorbed by each sample is the average solar absorptance (A), defined as:

$$A = \frac{\int_{300nm}^{2000nm} A(\lambda)\hat{\mathrm{A}}\cdot I(\lambda)d\lambda}{\int_{300nm}^{2000nm} A(\lambda)d\lambda} \quad (2)$$

where λ stands for the wavelength of the radiation, $A(\lambda)$ is the spectral absorptance, and $I(\lambda)$ is the AM1.5G spectral solar irradiance of the sun reaching the Earth's surface. As shown in Fig. 5b, albero samples exhibit a much higher value of absorptance as compared to limestone, which

Fig. 4. Pictures of the samples of albero (before and after calcination) and limestone.

would facilitate their calcination by the direct incidence of solar radiation. These results are the key to this work: the average solar absorptance increases from 6.15 % to 46.28 % and 53.37 %, what constitute an enhancement of 752 % and 868 % for garbancillo and grancilla, respectively. The reddish color of albero contributes to the increase of the solar absorptivity. This further emphasizes that this is a promising material for TCES.

The emissivity (ε) of the samples measured with the optris PI 450i infrared camera is presented as a function of temperature in Fig. S2. The total emissivity was measured for sample temperatures from 200 °C to 650 °C, taking into account Kirchoffs law of thermal radiation. In general, emissivity decreases as temperature increases. This is because the blackbody spectrum shifts towards lower wavelength values as the temperature increases, where the spectral absorbance is also lower. This is most noticeable at elevated temperatures. In the range in which the measurements were made, the emissivity can be assumed as almost constant. Thus, it appears that the emissivity of the albero samples decreases from approximately 1 to about 0.9 as the temperature increases from 200 °C to 650 °C. On the other hand, the emissivity of limestone initially decreases and then slightly increases with temperature. Interestingly, the emissivity is higher for albero than for limestone in the whole temperature range.

3.2. Multicycle Calcium-Looping performance

Fig. 6 shows the thermograms of the multicycle experiments conducted under conditions corresponding to the two different schemes proposed for CaL-CSP. The multicycle tests included in Fig. 6a and Fig. 6b correspond to CSP-N_2-calc conditions for garbancillo and grancilla, respectively.

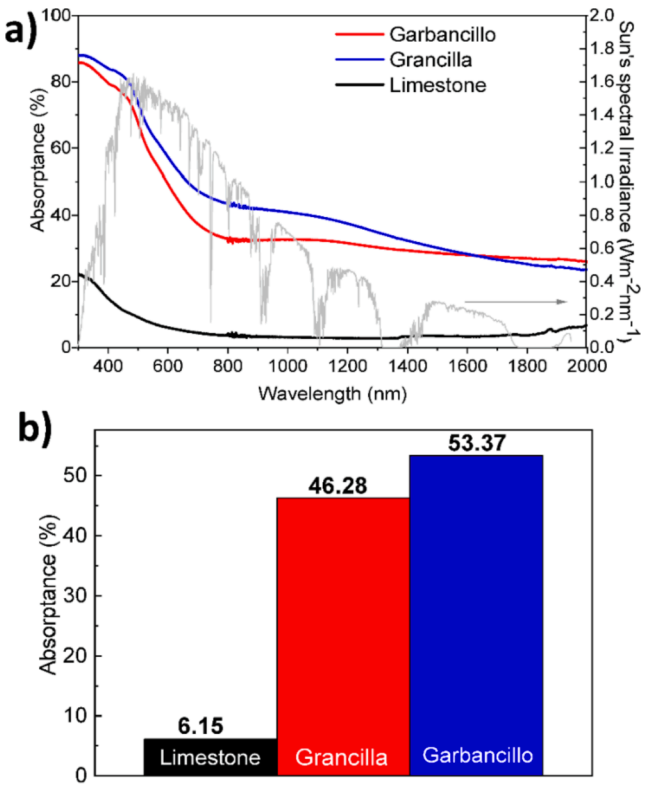

Fig. 5. a) Spectral absorptance of the samples of albero (heated at 500 °C) and limestone, and spectral irradiance of the sun reaching the earth surface (AM1.5G). b) Average solar absorptance of limestone, grancilla and garbancillo calculated from Eq. (2).

On the other hand, the results depicted in Fig. 6c and Fig. 6d correspond to CSP-CO_2-calc conditions, obtained for garbancillo and grancilla, respectively. As may be seen in Fig. 6c calcination of garbancillo is not fully attained in the first cycle. The thermograms are presented in terms of effective conversion, which is calculated as the ratio of the mass of CaO converted to $CaCO_3$ (being $m_{carb}(t)$ the sample mass at the time t) to the total mass of the sample m (including thus inert solids present in the sample) before carbonation. Therefore, $m_{carb}(t) - m$ is the CO_2 uptake during carbonation ($m_{CO_2}(t)$):.

$$X_{eff} = \frac{(m_{carb}(t) - m)}{m}\frac{W_{CaO}}{W_{CO_2}} = \frac{m_{CO_2}(t)}{m}\frac{W_{CaO}}{W_{CO_2}} \quad (3)$$

W_{CaO} and W_{CO_2} are the molar masses of CaO and CO_2, respectively. Assessing effective conversion X_{eff} instead of CaO conversion X is important for practical purposes. Due to the presence of inert solids in the sample, X_{eff} will be always smaller than X but these solids must be circulated through the cycle and therefore take a toll to efficiency and must be considered.

As expected, a progressive loss of conversion with the cycle number is observed in both experimental conditions, arguably caused by particle sintering as has been shown in previous works for limestone [12,59,60]. CSP-CO_2-calc tests involve harsher conditions than CSP-N_2-calc, since calcination at 950 °C in CO_2 has been previously demonstrated to strongly promote sintering. [25,60,61]. Thus, the values of effective conversion attained in CSP-CO_2-calc conditions are typically lower than those attained in CSP-N_2-calc conditions.

Fig. 7 shows data of effective conversion at the end of the carbonation stage X_{eff} as a function of the cycle number measured under CSP-N_2-calc conditions and CSP-CO_2-calc conditions. The results have been compared with those of a limestone sample with a particle size of 30 μm, tested under the same conditions [28].

As already seen in Fig. 6, the effective conversion is higher for the

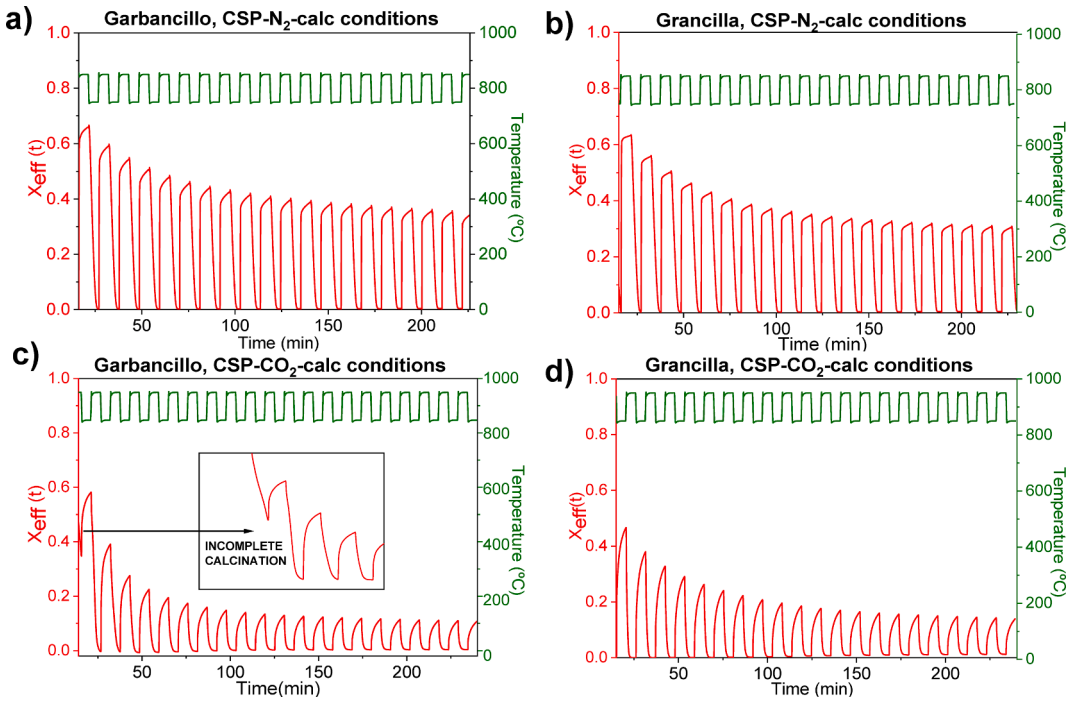

Fig. 6. Time evolution of temperature and effective conversion for multicycle CaL tests conducted under CSP-N_2-calc conditions and CSP-CO_2-calc conditions.

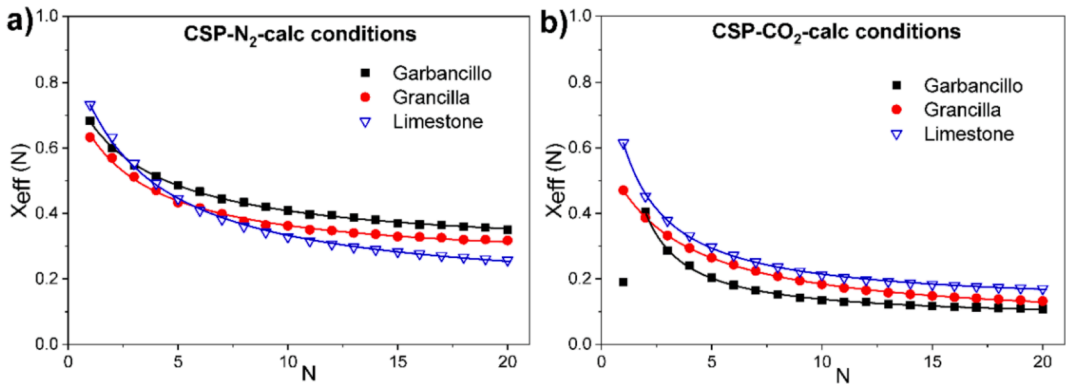

Fig. 7. Multicycle effective conversion of samples under CSP-N_2-calc conditions and CSP-CO_2-calc conditions.

tests performed under CSP-N_2-calc conditions than under CSP-CO_2-calc conditions. The optimal conditions for energy storage in CSP would be those that maximise the discharge temperature to improve the efficiency of the thermodynamic cycle, while avoiding excessive deactivation of the sorbent. The poor value of conversion attained by garbancillo at the first cycle in CSP-CO_2-calc conditions is due to uncompleted calcination. In CSP-N_2-calc conditions, garbancillo exhibits better performance, while in CSP-CO_2-calc conditions, this trend inverts. Interestingly, higher effective conversion values are obtained for the albero samples than for limestone tested under CSP-N_2-calc conditions, but the opposite is found when the tests are carried out in CSP-CO_2-calc conditions. This could be explained by the presence of silica in albero, which has been demonstrated to negatively affect the multicycle performance when calcination is carried out at high temperatures [62].

Data of conversion can be well fitted using the following expression [48,63,64]:.

$$X_{eff,N} = \frac{X_{eff,1}}{k(N-1) + \left(1 - X_{eff,r}/X_{eff,1}\right)^{-1}} \quad (4)$$

being N the cycle number, k the deactivation constant, $X_{eff,r}$ the residual conversion and $X_{eff,1}$ the value of conversion in the first cycle. Conversion converges asymptotically towards its residual number after many cycles. As the material must be repeatedly cycled over, this is the most relevant parameter for practical purposes. Since calcination is not fully attained in the first cycle for garbancillo in CSP-CO_2-calc conditions, this point has not been considered in the fitting. Best-fitting parameters are collected in Table 3. The values of R^2 obtained very close to one demonstrate that data can be quite well fitted using Eq. (4).

The time evolution of effective conversion measured for grancilla during the first cycle under CSP-N_2-calc and CSP-CO_2-calc conditions is plotted in Fig. 8. As may be seen two carbonation phases can be well differentiated as reported in previous works for a wide variety of Ca based materials [48,65]. First, carbonation occurs in a relatively fast phase on the particles' surface. This reaction-controlled phase is just limited by the kinetics of the carbonation reaction. The value of conversion attained at the end of the reaction-controlled phase strongly depends on the CaO surface area readily available for carbonation. Once the fast reaction-controlled phase is completed, carbonation is limited by solid-state diffusion of CO_2 through the $CaCO_3$ layer built upon the CaO particles' surface in the first phase [65,66]. Carbonation during the diffusion-controlled phase is notably slower as compared to the reaction-

Table 3
Residual conversion ($X_{eff,r}$), deactivation constant (k) and R-squared (R^2) values obtained by fitting Eq. (4) to experimental data measured for the samples under CSP-N_2-calc and CSP-CO_2-calc conditions.

	CSP-N_2-calc conditions			CSP-CO_2-calc conditions		
	Grancilla	Garbancillo	Limestone	Grancilla	Garbancillo	Limestone
$X_{eff,r}$	0.245	0.283	0.145	0.057	0.032	0.115
k	0.407	0.419	0.298	0.285	0.277	0.417
R^2	0.996	0.999	0.999	0.999	0.999	0.999

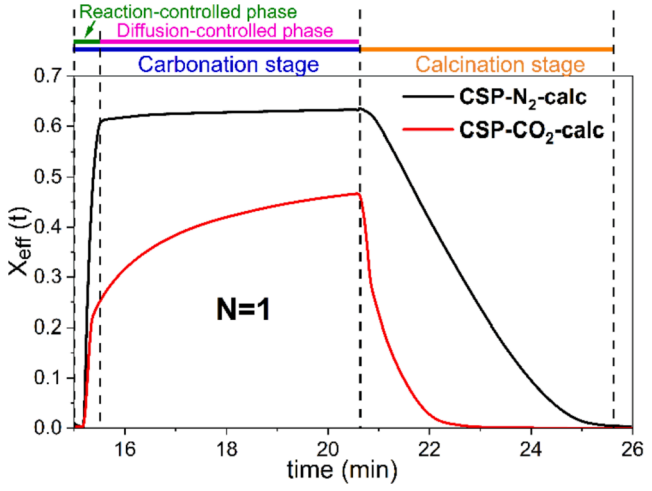

Fig. 8. Time evolution of effective conversion measured for grancilla during the first cycle under CSP-N_2-calc (black line) and CSP-CO_2-calc (red line) conditions.

controlled phase as can be seen in Fig. 8. Analyzing the kinetics of carbonation in both phases is relevant for practical purposes since it may affect the efficiency of the technology as depending on the solids residence time on the carbonator [67].

The contribution to the overall conversion of the fast reaction-controlled phase ($X_{eff,RC}$) and diffusion-controlled phase ($X_{eff,DC}$) is critically affected by the CaL conditions employed as can be clearly seen in Fig. 8. Fig. 9 shows multicycle data of $X_{eff,RC}$ and $X_{eff,DC}$ derived from the tests carried out under CSP-N_2-calc and CSP-CO_2-calc conditions in our work. In the tests performed under CSP-N_2-calc conditions, most of the CaO is converted during the reaction-controlled phase and the mass gained during the diffusion-controlled phase is negligible. However, under CSP-CO_2-calc conditions conversion in both phases is similar. CSP-CO_2-calc conditions strongly promotes sintering of the unreacted CaO during calcination under CO_2, which leads to a significant reduction in the surface area available. Consequently, this fraction of CaO loses reactivity towards carbonation in the next cycle, which progressively hinders conversion in the reaction-controlled phase. On the other hand, the lower temperatures employed in the calcination stage under CSP-N_2-calc conditions mitigate sintering of the unreacted CaO, which therefore preserves a significant reactivity for carbonation in the next cycle. Thus, conversion in the reaction-controlled stage is kept relatively high under these conditions.

Structural changes experienced by the samples during the multicycle carbonation/calcination tests were studied by recording X-ray diffractograms of the samples after being subjected to 20 cycles under both CSP-N_2-calc and CSP-CO_2-calc conditions, ending in carbonation (Fig. 10). The same phases are obtained for both albero samples after the tests. Thus, calcite and unreacted CaO are the main phases present.

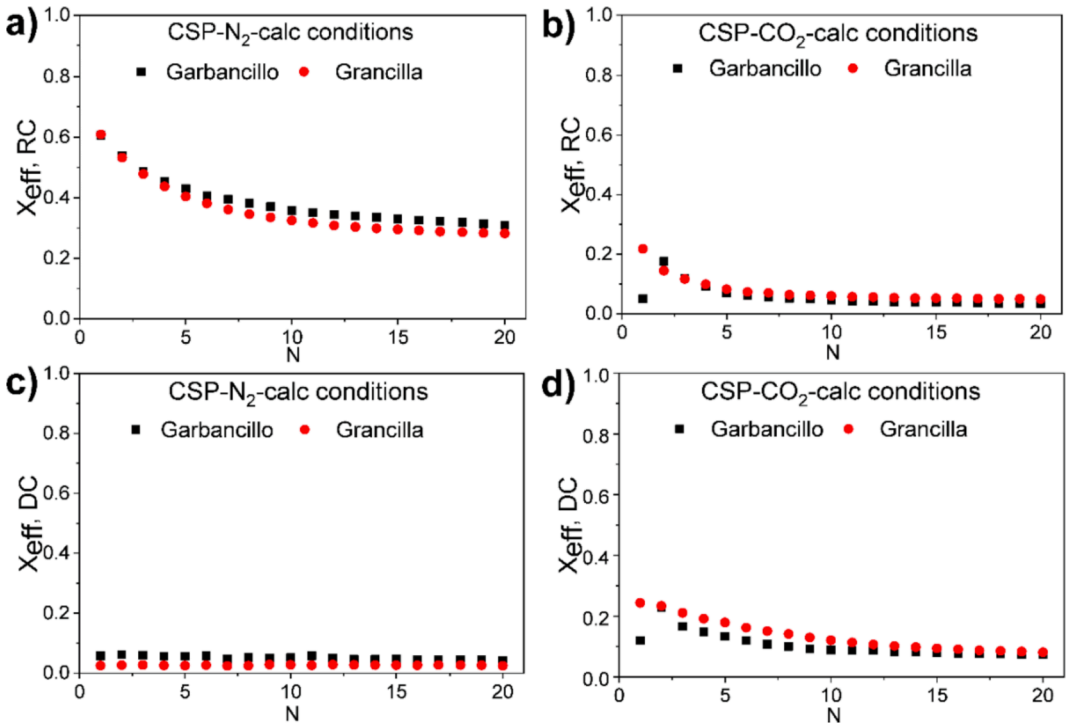

Fig. 9. a) and b): Effective conversion measured for the samples of albero in the reaction-controlled phase ($X_{eff,RC}$). c) and d): Effective conversion measured in the diffusion-controlled phase ($X_{eff,DC}$). Results are shown for the tests carried out under CSP-N_2-calc and CSP-CO_2-calc conditions.

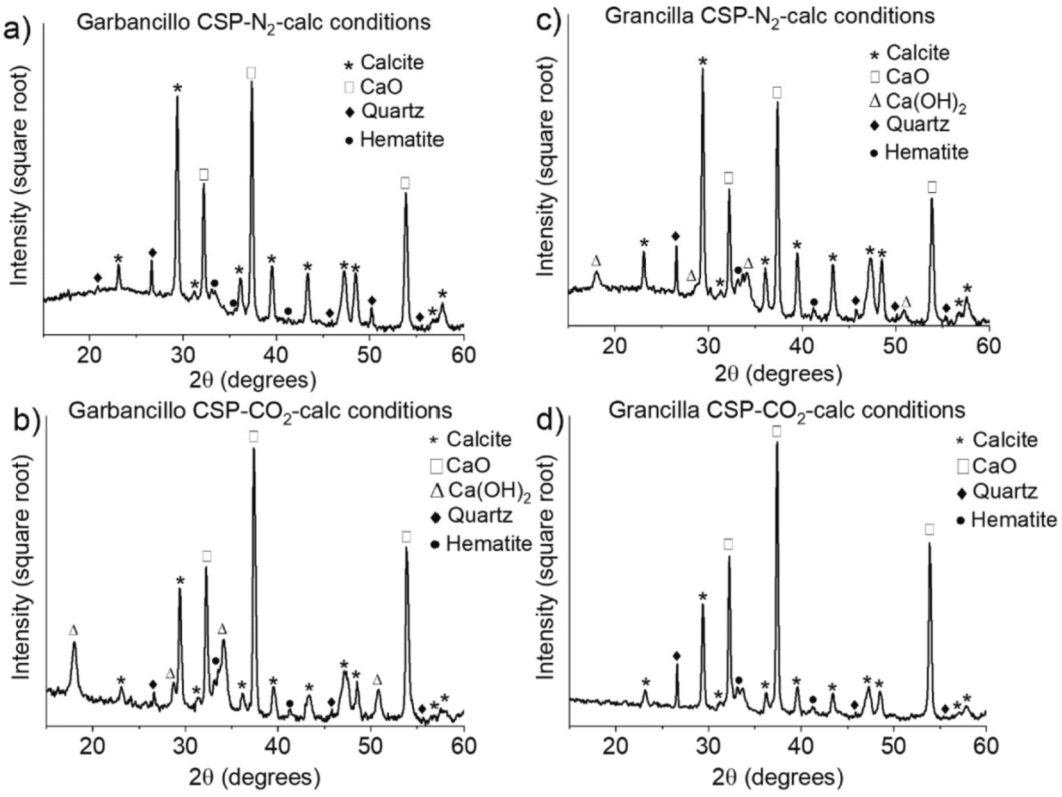

Fig. 10. X-ray diffraction patterns of the samples after twenty cycles performed under the CSP-N_2-calc (a, c) and CSP-CO_2-calc (b, d) conditions, ending in carbonation.

Quartz and small amounts of hematite can also be identified. Hematite forms after goethite dehydration during the cycles. Small amounts of $Ca(OH)_2$ are also detected, probably due to the rapid hydroxylation of CaO when the material is exposed to air. It is clear from the relative intensity of the $CaCO_3$ and CaO XRD peaks that the amount of unreacted CaO is much higher for the samples cycled under CSP-CO_2-calc conditions than for the samples cycled under CSP-N_2-calc conditions, which is in agreement with the results presented in Figs. 6-9. This can be related with the harsh calcination conditions used in the CSP-CO_2-CaL tests, which promote sintering of the material.

The impact of cycling on the samples' microstructure was studied using scanning electron microscopy. The micrographs in Fig. 11 show the particles' surface after 20 cycles conducted under CSP-N_2-calc and CSP-CO_2-calc conditions, ending in carbonation as $CaCO_3$ (Fig. 11 a, b, e and f) and in calcination as CaO (Fig. 11c, d, g and h). As CSP-CO_2-calc conditions entail the use of high CO_2 concentration and therefore higher calcination temperatures, sintering is expected to be more intense in these conditions. This is confirmed by the SEM micrographs and becomes clear by the presence of large grains of $CaCO_3$ in the samples cycled under CSP-CO_2-calc conditions. The shape of those grains is preserved when $CaCO_3$ transform into CaO under CSP-N_2-calc conditions, as can be observed in Fig. 11 c and g. However, this shape memory effect is not so clear for the samples calcined in CO_2. Fig. 11 c allows observing the interior of a particle through a crack on its surface. As can be observed, the interior remains more porous, which indicates that sintering mainly occurs on the surface. The conclusions of this analysis demonstrates that sintering is further promoted in CSP-CO_2-calc conditions.

3.3. Considerations of the application of the material in CaL-CSP plants. Scaling-up impact

Fig. 5 shows how the average solar absorptance increases from 6.15 % to 46.28 % and 53.37 % for garbancillo and grancilla, respectively. The higher absorptivity would reduce the losses linked to the non-absorbed radiation and reflections significantly, simplifying reactor designs and increasing the optical efficiency of the receiver, two of the main challenges of the CaL-CSP technology. Considering the effective conversion values at 20 cycles as representative of mean operation, Table 4 presents the estimated efficiencies for the plant presented in reference [5], the solar-to-heat efficiency, the global system efficiency, the energy storage capacity and the energy storage density of the materials.

The global system efficiency was calculated by multiplying the estimated efficiency of the plant and the solar-to-heat efficiency (η), which was obtained from Eq. (5):

$$\eta = a_s - \frac{\varepsilon\,(T)\;\sigma\;\left(T^4 - T_0^4\right)}{Q_s} \tag{5}$$

where a_s is the sun-weighted absorptance, $\varepsilon(T)$ is the emissivity at a temperature T, σ is the Stefan-Boltzmann constant, T_0 the ambient temperature and Q_s the concentrated incident solar radiation [49,68].

Moreover, the energy storage capacity of the materials (D_m, GJ/t) and the energy storage densities (D_v, GJ/m^3) were obtained from the following equations:

$$D_m = \Delta H_R^0 \times \left(\frac{m_{CO_2}}{m}\right)_r \tag{6}$$

$$D_v = D_m \times \rho \tag{7}$$

where ΔH_R^0 is the reaction enthalpy in kJ/kg CO_2 (4045,5 kJ/kg) and $\left(\frac{m_{CO_2}}{m}\right)_r$ is the CO_2 mass uptake divided by the mass of the sample before carbonation for the residual conversion, $X_{eff,r}$. This ratio is calculated from the values presented in Table 3 and Eq. (3). In Eq. (7), ρ is the density of the calcined materials, which consists essentially of CaO,

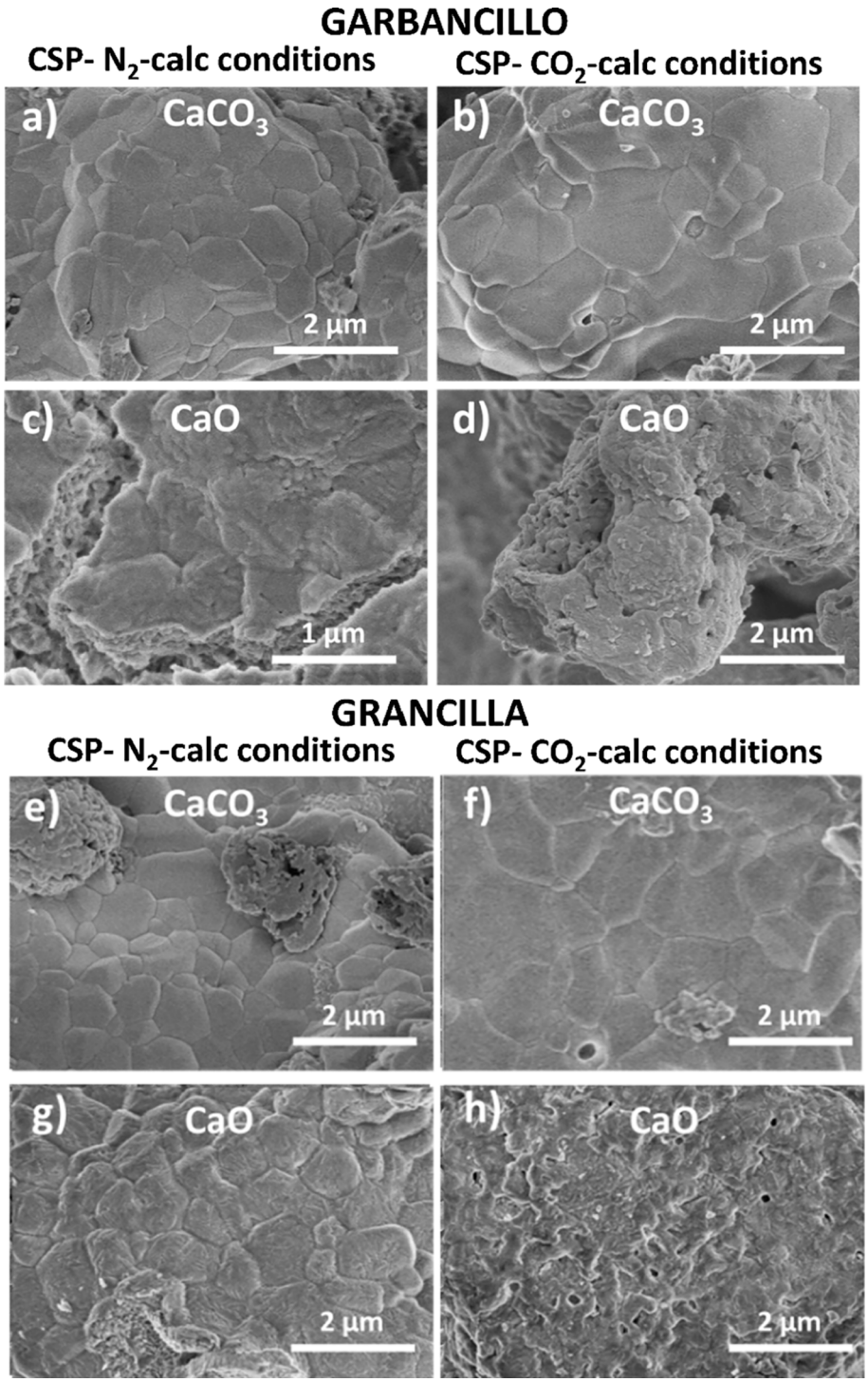

Fig. 11. SEM micrographs of the samples after 20 carbonation/calcination cycles performed under CSP-N_2-calc and CSP-CO_2-calc conditions, ending in carbonation (a, b, e and f) and ending in calcination (c, d, g and h).

quartz and iron oxide for the albero samples and CaO for limestone. Considering these compositions the corresponding densities of calcined grancilla, garbancillo and limestone are 3380, 3358 and 3340 kg/m^3, respectively.

These results show relatively similar efficiencies for the three materials (the two albero samples and limestone) independently of the CaL-CSP conditions. Higher efficiencies are obtained under CSP-CO_2-cal conditions despite the lower conversion values because of higher temperatures in the calciner and higher heat recovery under the operation conditions. These values do not include the effect on receiver efficiency and size, requiring a specific design. However, from these analyses it is derived that the expected increase in receiver efficiency due to the optical properties of the albero samples will result in similar global efficiency values for both CaL-CSP conditions.

Finally, since in the real application the material is expected to be used in a very large number of carbonation/calcionation cycles, the accumulated stored energy (ASE, in kJ/kg) of albero and limestone samples has been estimated for CSP-N_2-calc and CSP-CO_2-calc conditions from the values of energy storage capacity. Thus, for a large number of cycles ASE can be defined as:

Table 4
Plant estimated efficiency, solar-to-heat efficiency (η), global system efficiency, energy storage capacity and energy storage density, depending on the material and the calcination/carbonation conditions.

	CSP-N_2-calc conditions			CSP-CO_2-calc conditions		
	Grancilla	Garbancillo	Limestone	Grancilla	Garbancillo	Limestone
Plant Estimated efficiency (%)	34.5	34.8	33.8	39.2	38.3	40.9
η	0.46	0.53	0.06	0.46	0.53	0.06
Global system efficiency (%)	15.87	18.44	2.03	18.03	20.29	2.45
D_m(GJ/t)	0.78	0.90	0.46	0.18	0.10	0.37
D_v (GJ/m^3)	2.63	3.02	1.54	0.61	0.34	1.22

$$ASE\ (MJ/kg) = D_m \cdot N$$

where N is the number of cycles. The results obtained from this calculation are shown in Fig. 12 for up to 1000 cycles. This plot represents how a slight increase in residual conversion (which leads to the corresponding D_m values) drives to a significant increase in ASE. As expected, both the albero and limestone samples present a higher long-term ASE under CSP-N_2-calc conditions than under CSP-CO_2-calc conditions.

4. Conclusions

The use of a natural material so-called albero as a CaO precursor for thermochemical energy storage has been studied in this work. Albero is an abundant, cheap and non-toxic CaO precursor that presents a yellowish color due to the presence of small amounts of goethite that after calcination converts into hematite, producing a chromatic change to brown-reddish. It is demonstrated in this work that this natural material, used without any previous chemical treatment, presents a much higher solar absorptance than limestone (an improvement of 752%-868% depending on the sample), which would ease its calcination by the direct incidence of solar radiation. This is an important result since it opens the possibility of using direct solar absorption technologies in the CaL application to store energy in CSP plants.

The multicycle performance of the two albero samples (garbancillo and grancilla) at CaL conditions for thermochemical energy storage has been investigated considering two CaL-CSP schemes differing in the calcination stage. Thus, in the CSP-N_2-calc conditions, calcinations are performed under a nitrogen atmosphere, while for CSP-CO_2-calc conditions calcinations are carried out under CO_2. As expected, a variation in the calcination conditions has an important influence on the effective conversion of the albero samples. Multicycle effective conversions are higher for the samples subjected to carbonation/calcination cycles under CSP-N_2-calc conditions due to the softer calcination conditions employed, as compared to CSP-CO_2-calc, which prevents the sintering of the material.

Under both CaL-CSP schemes, CaO deactivation of the albero samples follows a similar trend and effective conversion values than limestone. Therefore, comparable residual conversions are obtained. Moreover, as also previously observed for limestone, carbonation in the fast reaction controlled phase plays the main role on the multicycle CaO conversion in the CSP-N_2-calc tests, due to the high surface area available, and the solid-state diffusion phase is negligible. On the other hand, carbonation in the solid-state diffusion phase is significant for the samples tested under CSP-CO_2-calc conditions, due to the marked sintering of CaO that decreases the surface area. Finally, the estimated efficiency under CSP-N_2-calc and CSP-CO_2-calc conditions was 34.5 and 39.2 % for grancilla, 34.8 and 38.3 % for garbancillo and 33.8 and 40.9 % for limestone. Moreover, the global system efficiency of the plant was calculated taking into account the solar-to-heat efficiency of the material. The results were 15.87 and 18.03 % for grancilla and 18.44 and 20.29 % for garbancillo under CSP-N_2-calc and CSP-CO_2-calc conditions, respectively. For limestone, these values were 2.03 and 2.45 % under CSP-N_2-calc and CSP-CO_2-calc conditions, respectively.

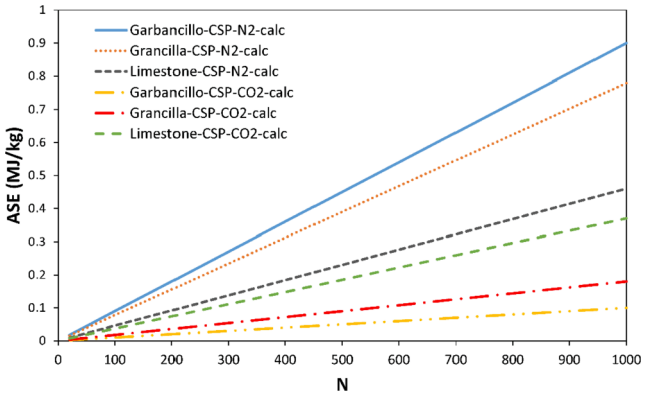

Fig. 12. Accumulated stored energy (ASE) of limestone and the albero samples, under CSP-N_2-calc and CSP-CO_2-calc conditions, as a function of the cycle number.

Declaration of Competing Interest

The authors declare that they have no known competing financial interests or personal relationships that could have appeared to influence the work reported in this paper.

Acknowledgments

This work has been funded by the grants CTQ2017-83602- C2-1-R and -2-R (MCIN/AEI/ 10.13039/501100011033 and ERDF A way of making Europe by the European Union), and grant PDC2021-121552-C21 (MCIN/AEI /10.13039/501100011033 and European Union Next Generation EU/PRTR). Financial support from projects P18-FR-1087 and US-1262507 (Junta de Andalucía-Consejería de Conocimiento, Investigación y Universidad-Fondo Europeo de Desarrollo Regional, Programa Operativo FEDER Andalucía 2014–2020) and INTRAMURAL-CSIC grant numbers 201960E092 and 202060I004 is acknowledged.

Appendix A. Supplementary data

Supplementary data to this article can be found online at https://doi.org/10.1016/j.cej.2022.135707.

References

[1] E. Commission, COM(2020) 741 final - An EU Strategy to harness the potential of offshore renewable energy for a climate neutral future, (2020).
[2] M. J. Pickl, The renewable energy strategies of oil majors – From oil to energy?, Energy Strategy Reviews 26 (2019) 100370 100370.
[3] J. Rogelj, M. Den Elzen, N. Höhne, T. Fransen, H. Fekete, H. Winkler, R. Schaeffer, F. Sha, K. Riahi, M. Meinshausen, Paris Agreement climate proposals need a boost to keep warming well below 2 °C, Nature 534 (7609) (2016) 631–639.
[4] W. Grace, in *Transition Towards 100% Renewable Energy: Selected Papers from the World Renewable Energy Congress WREC 2017*, ed. A. Sayigh, Springer International Publishing, Cham, 2018, DOI: 10.1007/978-3-319-69844-1_15, pp. 157-170.
[5] R. Chacartegui, A. Alovisio, C. Ortiz, J.M. Valverde, V. Verda, J.A. Becerra, Thermochemical energy storage of concentrated solar power by integration of the calcium looping process and a CO_2 power cycle, Appl. Energy 173 (2016) 589–605.

[6] C. Ortiz, J.M. Valverde, R. Chacartegui, L.A. Perez-Maqueda, P. Giménez, The calcium-looping ($CaCO_3$/CaO) process for thermochemical energy storage in Concentrating Solar Power plants, Renew. Sustain. Energy Rev. 113 (2019), 109252.

[7] P. Pardo, A. Deydier, Z. Anxionnaz-Minvielle, S. Rougé, M. Cabassud, P. Cognet, A review on high temperature thermochemical heat energy storage, Renew. Sustain. Energy Rev. 32 (2014) 591–610.

[8] A. Perejón, L.M. Romeo, Y. Lara, P. Lisbona, A. Martínez, J.M. Valverde, The calcium-Looping technology for CO_2 capture: On the important roles of energy integration and sorbent behavior, Appl. Energy 162 (2016) 787–807.

[9] M. Sarvghad, S. Delkasar Maher, D. Collard, M. Tassan, G. Will, T.A. Steinberg, Materials compatibility for the next generation of Concentrated Solar Power plants, Energy Storage Mater. 14 (2018) 179–198.

[10] F. Di Lauro, C. Tregambi, F. Montagnaro, P. Salatino, R. Chirone, R. Solimene, Improving the performance of calcium looping for solar thermochemical energy storage and CO_2 capture, Fuel 298 (2021), 120791.

[11] C. Tregambi, F. Di Lauro, F. Montagnaro, P. Salatino, R. Solimene, 110th Anniversary: Calcium Looping Coupled with Concentrated Solar Power for Carbon Capture and Thermochemical Energy Storage, Ind. Eng. Chem. Res. 58 (47) (2019) 21262–21272.

[12] M. Benitez-Guerrero, J.M. Valverde, P.E. Sanchez-Jimenez, A. Perejon, L.A. Perez-Maqueda, Multicycle activity of natural $CaCO_3$ minerals for thermochemical energy storage in Concentrated Solar Power plants, Sol. Energy 153 (2017) 188–199.

[13] J. Cot-Gores, A. Castell, L.F. Cabeza, Thermochemical energy storage and conversion: A-state-of-the-art review of the experimental research under practical conditions, Renew. Sustain. Energy Rev. 16 (2012) 5207–5224.

[14] N. Yu, R.Z. Wang, L.W. Wang, Sorption thermal storage for solar energy, Prog. Energy Combust. Sci. 39 (5) (2013) 489–514.

[15] B. Sarrión, A. Perejón, P.E. Sánchez-Jiménez, L.A. Pérez-Maqueda, J.M. Valverde, Role of calcium looping conditions on the performance of natural and synthetic Ca-based materials for energy storage, J. CO2 Util. 28 (2018) 374–384.

[16] S. Bai, Y. Zhou, Y. Chen, Z. Wang, J. Sun, C. Zhao, Thermochemical Energy Storage Performances of Steel Slag-Derived CaO-Based Composites, Chem. Eng. Technol. 43 (11) (2020) 2190–2197.

[17] M. Chawla, H. Saulat, M. Masood Khan, M. Mahmood Khan, S. Rafiq, L. Cheng, T. Iqbal, M.I. Rasheed, M.Z. Farooq, M. Saeed, N.M. Ahmad, M.B. Khan Niazi, S. Saqib, F. Jamil, A. Mukhtar, N. Muhammad, Membranes for CO_2/CH_4 and CO_2/N_2 Gas Separation, Chem. Eng. Technol. 43 (2) (2020) 184–199.

[18] Y. Da, Y. Xuan, L. Teng, K. Zhang, X. Liu, Y. Ding, Calcium-based composites for direct solar-thermal conversion and thermochemical energy storage, Chem. Eng. J. 382 (2020), 122815.

[19] H.C. Mantripragada, E.S. Rubin, Calcium looping cycle for CO_2 capture: Performance, cost and feasibility analysis, Energy Procedia 63 (2014) 2199–2206.

[20] J. Arcenegui-Troya, P.E. Sánchez-Jiménez, A. Perejón, J.M. Valverde, R. Chacartegui, L.A. Pérez-Maqueda, Calcium-Looping Performance of Biomineralized $CaCO_3$ for CO_2 Capture and Thermochemical Energy Storage, Ind. Eng. Chem. Res. 59 (29) (2020) 12924–12933.

[21] N. Asikin-Mijan, H.V. Lee, Y.H. Taufiq-Yap, G. Abdulkrem-Alsultan, M.S. Mastuli, H.C. Ong, Optimization study of SiO_2-Al_2O_3 supported bifunctional acid–base NiO-CaO for renewable fuel production using response surface methodology, Energy Convers. Manage. 141 (2017) 325–338.

[22] M. Benitez-Guerrero, J.M. Valverde, A. Perejon, P.E. Sanchez-Jimenez, L.A. Perez-Maqueda, Low-cost Ca-based composites synthesized by biotemplate method for thermochemical energy storage of concentrated solar power, Appl. Energy 210 (2018) 108–116.

[23] L.M. Romeo, J.C. Abanades, J.M. Escosa, J. Paño, A. Giménez, A. Sánchez-Biezma, J.C. Ballesteros, Oxyfuel carbonation/calcination cycle for low cost CO_2 capture in existing power plants, Energy Convers. Manage. 49 (10) (2008) 2809–2814.

[24] J.K. Stolaroff, G.V. Lowry, D.W. Keith, Using CaO- and MgO-rich industrial waste streams for carbon sequestration, Energy Convers. Manage. 46 (5) (2005) 687–699.

[25] J. Blamey, E.J. Anthony, J. Wang, P.S. Fennell, The calcium looping cycle for large-scale CO_2 capture, Prog. Energy Combust. Sci. 36 (2) (2010) 260–279.

[26] P. Sun, J.R. Grace, C.J. Lim, E.J. Anthony, The effect of CaO sintering on cyclic CO_2 capture in energy systems, AIChE J. 53 (9) (2007) 2432–2442.

[27] M. Benitez-Guerrero, B. Sarrion, A. Perejon, P.E. Sanchez-Jimenez, L.A. Perez-Maqueda, J. Manuel Valverde, Large-scale high-temperature solar energy storage using natural minerals, Sol. Energy Mater. Sol. Cells 168 (2017) 14–21.

[28] J.D. Durán-Martín, P.E. Sánchez Jimenez, J.M. Valverde, A. Perejón, J. Arcenegui-Troya, P. García Triñanes, L.A. Pérez Maqueda, Role of particle size on the multicycle calcium looping activity of limestone for thermochemical energy storage, J. Adv. Res. 22 (2020) 67–76.

[29] H. Sun, Y. Li, Z. Bian, X. Yan, Z. Wang, W. Liu, Thermochemical energy storage performances of Ca-based natural and waste materials under high pressure during CaO/$CaCO_3$ cycles, Energy Convers. Manage. 197 (2019), 111885.

[30] D.P. Hanak, M. Erans, S.A. Nabavi, M. Jeremias, L.M. Romeo, V. Manovic, Technical and economic feasibility evaluation of calcium looping with no CO_2 recirculation, Chem. Eng. J. 335 (2018) 763–773.

[31] M. Benitez-Guerrero, J.M. Valverde, P.E. Sanchez-Jimenez, A. Perejon, L.A. Perez-Maqueda, Calcium-Looping performance of mechanically modified Al_2O_3-CaO composites for energy storage and CO_2 capture, Chem. Eng. J. 334 (2018) 2343–2355.

[32] J. Chen, L. Duan, Z. Sun, Accurate Control of Cage-Like CaO Hollow Microspheres for Enhanced CO_2 Capture in Calcium Looping via a Template-Assisted Synthesis Approach, Environ. Sci. Technol. 53 (4) (2019) 2249–2259.

[33] V. Manovic, P.S. Fennell, M.J. Al-Jeboori, E.J. Anthony, Steam-enhanced calcium looping cycles with calcium aluminate pellets doped with bromides, Ind. Eng. Chem. Res. 52 (23) (2013) 7677–7683.

[34] S. Champagne, D.Y. Lu, A. MacChi, R.T. Symonds, E.J. Anthony, Influence of steam injection during calcination on the reactivity of CaO-based sorbent for carbon capture, Ind. Eng. Chem. Res. 52 (6) (2013) 2241–2246.

[35] J. Arcenegui-Troya, P.E. Sánchez-Jiménez, A. Perejón, V. Moreno, J.M. Valverde, L.A. Pérez-Maqueda, Kinetics and cyclability of limestone ($CaCO_3$) in presence of steam during calcination in the CaL scheme for thermochemical energy storage, Chem. Eng. J. 417 (2021) 129194.

[36] J.S. De Sousa, V.N. Freire, E.L. Albuquerque, Electronic and optical properties of $CaCO_3$ porous nanoparticles, J. Appl. Phys. 100 (2006) 1–4.

[37] N.H. Sulimai, R.A. Rani, Z. Khusaimi, S. Abdullah, M.J. Salifairus, S. Alrokayan, H. Khan, P.A. Sermon, M. Rusop, Facile synthesis of $CaCO_3$ and investigation on structural and optical properties of high purity crystalline calcite, Materials Science and Engineering B: Solid-State Materials for Advanced Technology 243 (2019) 78–85.

[38] H. Zhan, S. Wu, K. Zhao, R. Bao, L. Xiao, $CaCO_3$, its reaction and carbonate rocks: Terahertz spectroscopy investigation, J. Geophys. Eng. 13 (2016) 768–774.

[39] M. Díaz-Heras, A. Calderón, M. Navarro, J.A. Almendros-Ibáñez, A.I. Fernández, C. Barreneche, Characterization and testing of solid particles to be used in CSP plants: Aging and fluidization tests, Sol. Energy Mater. Sol. Cells 219 (2021) 110793.

[40] C. Tregambi, F. Montagnaro, P. Salatino, R. Solimene, Directly irradiated fluidized bed reactors for thermochemical processing and energy storage: Application to calcium looping, AIP Conf. Proc. 1850 (1) (2017), 090007.

[41] G. Flamant, D. Hernandez, C. Bonet, J.-P. Traverse, Experimental aspects of the thermochemical conversion of solar energy; Decarbonation of CaCO3, Sol. Energy 24 (4) (1980) 385–395.

[42] T. Esence, E. Guillot, M. Tessonneaud, J.-L. Sans, G. Flamant, Solar calcination at pilot scale in a continuous flow multistage horizontal fluidized bed, Sol. Energy 207 (2020) 367–378.

[43] T. Esence, H. Benoit, D. Poncin, M. Tessonneaud, G. Flamant, A shallow cross-flow fluidized-bed solar reactor for continuous calcination processes, Sol. Energy 196 (2020) 389–398.

[44] M.E. Diego, B. Arias, J.C. Abanades, Evolution of the CO_2 carrying capacity of CaO particles in a large calcium looping pilot plant, Int. J. Greenhouse Gas Control 62 (2017) 69–75.

[45] I. Martínez, G. Grasa, R. Murillo, B. Arias, J.C. Abanades, Modelling the continuous calcination of $CaCO_3$ in a Ca-looping system, Chem. Eng. J. 215–216 (2013) 174–181.

[46] J. Obermeier, K.G. Sakellariou, N.I. Tsongidis, D. Baciu, G. Charalambopoulou, T. Steriotis, K. Müller, G. Karagiannakis, A.G. Konstandopoulos, A. Stubos, W. Arlt, Material development and assessment of an energy storage concept based on the CaO-looping process, Sol. Energy 150 (2017) 298–309.

[47] C. Ortiz, R. Chacartegui, J.M. Valverde, J.A. Becerra, L.A. Perez-Maqueda, A new model of the carbonator reactor in the calcium looping technology for post-combustion CO_2 capture, Fuel 160 (2015) 328–338.

[48] J.M. Valverde, A model on the CaO multicyclic conversion in the Ca-looping process, Chem. Eng. J. 228 (2013) 1195–1206.

[49] C.K. Ho, B.D. Iverson, Review of high-temperature central receiver designs for concentrating solar power, Renew. Sustain. Energy Rev. 29 (2014) 835–846.

[50] E. Karasavvas, K.D. Panopoulos, S. Papadopoulou, S. Voutetakis, Energy and exergy analysis of the integration of concentrated solar power with calcium looping for power production and thermochemical energy storage, Renewable Energy 154 (2020) 743–753.

[51] W.G. Le Roux, T. Bello-Ochende, J.P. Meyer, The efficiency of an open-cavity tubular solar receiver for a small-scale solar thermal Brayton cycle, Energy Convers. Manage. 84 (2014) 457–470.

[52] Z. Liao, X. Li, C. Xu, C. Chang, Z. Wang, Allowable flux density on a solar central receiver, Renewable Energy 62 (2014) 747–753.

[53] U. Tesio, E. Guelpa, C. Ortiz, R. Chacartegui, V. Verda, Energy Strategy Reviews, Energy Conversion and Management: X 4 (2019), 100025.

[54] C. Song, X. Liu, H. Zheng, C. Bao, L. Teng, Y. Da, F. Jiang, Decomposition kinetics of Al- and Fe-doped calcium carbonate particles with improved solar absorbance and cycle stability, Chem. Eng. J. 406 (2021), 126282.

[55] H. Chen, P. Zhang, Y. Duan, C. Zhao, Reactivity enhancement of calcium based sorbents by doped with metal oxides through the sol-gel process, Appl. Energy 162 (2016) 390–400.

[56] R. Sun, Y. Li, H. Liu, S. Wu, C. Lu, CO_2 capture performance of calcium-based sorbent doped with manganese salts during calcium looping cycle, Appl. Energy 89 (1) (2012) 368–373.

[57] L. Teng, Y. Xuan, Y. Da, X. Liu, Y. Ding, Modified Ca-Looping materials for directly capturing solar energy and high-temperature storage, Energy Storage Mater. 25 (2020) 836–845.

[58] H.D. Ruan, R.L. Frost, J.T. Kloprogge, The behavior of hydroxyl units of synthetic goethite and its dehydroxylated product hematite, Spectrochimica Acta - Part A: Molecular and Biomolecular Spectroscopy 57 (13) (2001) 2575–2586.

[59] K. Wang, F. Gu, P.T. Clough, P. Zhao, E.J. Anthony, Porous MgO-stabilized CaO-based powders/pellets via a citric acid-based carbon template for thermochemical energy storage in concentrated solar power plants, Chem. Eng. J. 390 (2020), 124163.

[60] P.E. Sánchez Jiménez, A. Perejón, M. Benítez Guerrero, J.M. Valverde, C. Ortiz, L. A. Pérez Maqueda, High-performance and low-cost macroporous calcium oxide based materials for thermochemical energy storage in concentrated solar power plants, Appl. Energy 235 (2019) 543–552.

[61] R.H. Borgwardt, Calcium Oxide Sintering in Atmospheres Containing Water and Carbon Dioxide, Ind. Eng. Chem. Res. 28 (4) (1989) 493–500.
[62] J.M. Valverde, J. Miranda-Pizarro, A. Perejón, P.E. Sánchez-Jiménez, L.A. Pérez-Maqueda, Calcium-Looping performance of steel and blast furnace slags for thermochemical energy storage in concentrated solar power plants, J. CO2 Util. 22 (2017) 143–154.
[63] G.S. Grasa, J.C. Abanades, CO_2 capture capacity of CaO in long series of carbonation/calcination cycles, Ind. Eng. Chem. Res. 5 (26) (2006) 8846–8851.
[64] J.M. Valverde, P.E. Sanchez-Jimenez, A. Perejon, L.A. Perez-Maqueda, CO_2 multicyclic capture of pretreated/doped CaO in the Ca-looping process, Theory and experiments, Physical Chemistry Chemical Physics 15 (2013) 11775–11793.
[65] Z. Sun, S. Luo, P. Qi, L.S. Fan, Ionic diffusion through Calcite ($CaCO_3$) layer during the reaction of CaO and CO_2, Chem. Eng. Sci. 81 (2012) 164–168.
[66] S.K. Bhatia, D.D. Perlmutter, Effect of the product layer on the kinetics of the CO_2-lime reaction, AIChE J. 29 (1) (1983) 79–86.
[67] C. Ortiz, J.M. Valverde, R. Chacartegui, Energy Consumption for CO_2 Capture by means of the Calcium Looping Process: A Comparative Analysis using Limestone, Dolomite, and Steel Slag, Energy Technology 4 (10) (2016) 1317–1327.
[68] M. Diago, A.C. Iniesta, A. Soum-Glaude, N. Calvet, Characterization of desert sand to be used as a high-temperature thermal energy storage medium in particle solar receiver technology, Appl. Energy 216 (2018) 402–413.